

Table 4. q -exponents in the ST phase. Analytically derived q -exponents for self-absorbed and optically thin synchrotron radiation in the ST phase. The quantities on the first column correspond to the different physical parameters on which the flux depends (see equation 18). Each column describes their values for a given power-law segment.

| | F_2 | $F_{5/2}$ | $F_{1/3}$ | $F_{(1-p)/2}$ |
|---------|---------------------|------------------------|-------------------------|----------------------------------|
| q_ξ | -1 | 0 | $\frac{5}{3}$ | $2-p$ |
| q_e | 1 | 0 | $-\frac{2}{3}$ | $p-1$ |
| q_B | 0 | $-\frac{1}{4}$ | $\frac{1}{3}$ | $\frac{p+1}{4}$ |
| q_n | $-\frac{4}{5-k}$ | $-\frac{11}{4(5-k)}$ | $\frac{13}{3(5-k)}$ | $\frac{19-5p}{4(5-k)}$ |
| q_E | $\frac{4}{5-k}$ | $\frac{6+k}{4(5-k)}$ | $\frac{7-4k}{3(5-k)}$ | $\frac{10p+6-k(p+5)}{4(5-k)}$ |
| q_v | 2 | $\frac{5}{2}$ | $\frac{1}{3}$ | $\frac{1-p}{2}$ |
| q_t | $\frac{2k-2}{5-k}$ | $\frac{11}{2(5-k)}$ | $\frac{24-10k}{3(5-k)}$ | $\frac{3(7-5p)+4k(p-2)}{2(5-k)}$ |
| q_z | $\frac{17-5k}{5-k}$ | $\frac{24-7k}{2(5-k)}$ | $\frac{6k-4}{3(5-k)}$ | $\frac{5(2p+k)-3(2+kp)}{2(5-k)}$ |

Table 5. g -factors in the ST phase. Numerically determined g -factors for self-absorbed and optically thin synchrotron radiation in the ST phase. The quantities on the first column correspond to different factors of the normalizing polynomial (see equation 19). Each column describes their values for a given power-law segment.

| | F_2 | $F_{5/2}$ | $F_{1/3}$ | $F_{(1-p)/2}$ |
|----------|---------|-----------|-----------|---------------|
| g_0 | -16.510 | -25.645 | -5.513 | -8.789 |
| g_p | 0 | 0 | 0 | 8.528 |
| g_{pp} | 0 | 0 | 0 | 0.230 |
| g_k | 0.126 | -0.017 | -0.044 | 0.157 |
| g_{kk} | -0.009 | -0.014 | 0.008 | 0.070 |

are presented in Table 4 while the factors of the calibrating polynomials are presented in Table 5. We note that the values of q_v and q_t are in agreement with those presented in Frail, Waxman & Kulkarni (2000), apart from their equation (A18) where the scaling for $\nu_{\text{obs}} \ll \nu_m$ is in error. This error appears also in van Eerten et al. (2010a).

3.5 The sharpness of spectral breaks

In practice the spectral breaks are not infinitely sharp as shown in Figs 1 and 2 but show a gradual transition from one power-law index to another. To complete our description of instantaneous spectra, we need to provide a formula for the sharpness of spectral breaks.

An approach commonly used (Granot & Sari 2002; van Eerten & Wijers 2009) is to describe the flux close to a break by the following equation (Beuermann et al. 1999):

$$F_\nu(\nu_{\text{obs}}) = A \left[\left(\frac{\nu_{\text{obs}}}{\nu_0} \right)^{-a_1 s} + \left(\frac{\nu_{\text{obs}}}{\nu_0} \right)^{-a_2 s} \right]^{-1/s}, \quad (22)$$

where (ν_0, A) are the coordinates of the meeting point of the two power laws associated with the break, a_1 and a_2 are the asymptotic power-law indices before and after the break, respectively, and s is the so called ‘sharpness parameter’. We have performed χ^2 -minimization fitting in logarithmic space to obtain values of s for specific runs and used those to arrive at a description of the sharpness in terms of a polynomial of p and k . This polynomial has the general

Table 6. s -factors in the BM phase. Numerically determined s -factors (see equation 23) for all possible breaks in the BM phase. Each column describes a specific break, with the two associated spectral indices denoted on top.

| | $2 \rightarrow \frac{5}{2}$ | $\frac{5}{2} \rightarrow \frac{1-p}{2}$ | $2 \rightarrow \frac{1}{3}$ | $\frac{1}{3} \rightarrow \frac{1-p}{2}$ |
|----------|-----------------------------|---|-----------------------------|---|
| s_0 | -2.91 | 1.24 | 1.64 | 1.83 |
| s_p | -0.11 | -0.145 | 0 | -0.41 |
| s_k | 0.04 | 0 | -0.18 | 0 |
| s_{kk} | 0 | 0 | 0 | 0 |

Table 7. s -factors in the ST phase. Numerically determined s -factors (see equation 23) for all possible breaks in the ST phase. Each column describes a specific break, with the two associated spectral indices denoted on top.

| | $2 \rightarrow \frac{5}{2}$ | $\frac{5}{2} \rightarrow \frac{1-p}{2}$ | $2 \rightarrow \frac{1}{3}$ | $\frac{1}{3} \rightarrow \frac{1-p}{2}$ |
|----------|-----------------------------|---|-----------------------------|---|
| s_0 | -5.50 | 3.50 | 2.63 | 1.88 |
| s_p | 0.73 | -0.71 | -0.24 | -0.46 |
| s_k | 0.10 | -0.07 | -0.31 | 0.11 |
| s_{kk} | 0 | -0.11 | -0.07 | -0.02 |

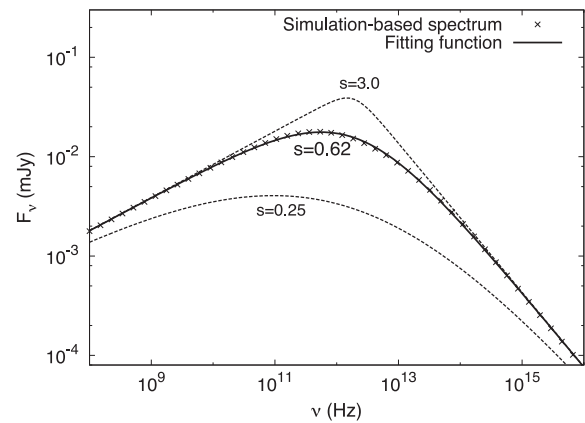


Figure 3. The effect of sharpness on the flux close to a spectral break. This fragment of the simulation-based spectrum focuses on the flux around ν_m . The best fit is shown along with two more curves that have the same parameters but different sharpness. Simulation-based spectrum has the following model parameters: $E_{52} = 1, n_0 = 1, p = 2.5, k = 0, \xi = 10^{-2}, \epsilon_e = 10^{-1}, \epsilon_B = 10^{-2}, d_{28} = 1, z = 0.56, t_{\text{obs}} = 100$ d.

form

$$s = s_0 + s_p p + s_k k + s_{kk} k^2. \quad (23)$$

Its factors have been determined by solving the system of equations resulting from the application of equation (22) to models with different p and k parameters. In Tables 6 and 7 we present the values of s_0, s_p, s_k and s_{kk} in the BM and the ST phase, respectively.

In Fig. 3 a best fit to the shape of the spectrum around ν_m is shown, for one of the run models. We also plot the flux for two different values of s to illustrate the notable effect it can have on flux levels.

4 THE TRANSRELATIVISTIC REGIME

The results of the previous section constitute a full description of the possible synchrotron spectra (ignoring cooling) during the ultra-relativistic and non-relativistic dynamical phases of the afterglow

evolution. However, we have not yet addressed a large portion of the afterglow's overall behaviour, namely the *transrelativistic* regime. During this stage the dynamics deviates considerably from the BM solution, without having settled yet into the ST solution. As mentioned in Section 1, this phase of the afterglow typically spans a few orders of magnitude in observer time, while there is no full description of its dynamics, even in the simple, spherical case.

An approach we have investigated and found useful is that of treating the transrelativistic phase as a 'break' during which the temporal evolution of the spectrum's critical parameters displays a smooth transition from the relativistic power-law behaviour to the non-relativistic one. These parameters could be, for example, the values of the flux at every possible power-law segment. However, the same level of accuracy can be achieved by using the positions of the critical frequencies and the flux at one of them, instead. Based on values for these parameters one can construct the spectrum (Sari et al. 1998; Wijers & Galama 1999) because the slopes of the power-law segments are known for a given ordering of ν_a and ν_m .

4.1 Peak flux

A convenient frequency to measure the flux is at ν_m of spectrum 1. This is because we can assume that the bulk of the electrons radiate most of their power at that frequency. Using equation (11) in combination with the scalings for the dynamics in each of the two extreme phases of the outflow, we find for the flux at ν_m

$$F_{m-BM} = C_{\text{pol}} \xi \epsilon_B^{\frac{1}{2}} n_0^{\frac{4}{2(4-k)}} E_{52}^{\frac{8-3k}{2(4-k)}} t_{\text{obs}}^{\frac{-k}{2(4-k)}} (1+z)^{\frac{8-k}{2(4-k)}} d_{28}^{-2}, \quad (24)$$

in the BM phase and

$$F_{m-ST} = C_{\text{pol}} \xi \epsilon_B^{\frac{1}{2}} n_0^{\frac{7}{2(5-k)}} E_{52}^{\frac{8-3k}{2(5-k)}} t_{\text{obs}}^{\frac{3-2k}{5-k}} (1+z)^{\frac{2+k}{5-k}} d_{28}^{-2}, \quad (25)$$

in the ST phase. The g -factors of C_{pol} for both dynamical phases are presented in Table 8.

4.2 Critical frequencies

The behaviour of the critical frequencies can easily be deduced (in either the BM or ST phase) by equating the flux formulas on both sides of a spectral break. For each of ν_m and ν_a there will be two such expressions corresponding to the two possible spectra for the two different orderings of the frequencies. In general, the value of a critical frequency will be given by the following formula

$$\nu_{\text{cr}} = f_n \xi^{q_\xi} \epsilon_e^{q_e} \epsilon_B^{q_B} n_0^{q_n} E_{52}^{q_E} \nu_{\text{obs}}^{q_\nu} t_{\text{obs}}^{q_t} (1+z)^{q_z}. \quad (26)$$

The numerical factors f_n result from equating the fluxes of the power laws at each side of the spectral break. Tables 9 and 10 summarize the formulas for the critical frequencies in the BM phase for the two different possible spectra. For the ST phase we repeat the same procedure and summarize our results in Tables 11 and 12.

Table 8. g -factors for F_{m-BM} and F_{m-ST} . Numerically determined g -factors for F_m (measured at ν_{m1}), both in the BM and ST phase.

| | F_{m-BM} | F_{m-ST} |
|----------|------------|------------|
| g_0 | 0.531 | -0.674 |
| g_p | 0.487 | 0.305 |
| g_{pp} | -0.060 | -0.019 |
| g_k | -0.291 | -0.055 |
| g_{kk} | 0.004 | 0.015 |

Table 9. f_n and q -exponents for critical frequencies in the BM phase, while $\nu_a < \nu_m$ (spectrum 1). The q -exponents carry the analytically derived dependencies, while the f_n -factors carry the flux-calibrating C_{pol} and $h(p)$ (see equation 18, 19 and 20).

| | ν_{a1} | ν_{m1} |
|---------|--|---|
| f_n | $\left(\frac{C_{1/3} h_{1/3}}{C_2 h_2}\right)^{3/5}$ | $\left(\frac{C_{(1-p)/2} h_{(1-p)/2}}{C_{1/3} h_{1/3}}\right)^{\frac{6}{3p-1}}$ |
| q_ξ | $\frac{8}{5}$ | -2 |
| q_e | -1 | 2 |
| q_B | $\frac{1}{5}$ | $\frac{1}{2}$ |
| q_n | $\frac{12}{5(4-k)}$ | 0 |
| q_E | $\frac{4-4k}{5(4-k)}$ | $\frac{1}{2}$ |
| q_t | $-\frac{3k}{5(4-k)}$ | $-\frac{3}{2}$ |
| q_z | $\frac{8k-20}{5(4-k)}$ | $\frac{1}{2}$ |

Table 10. f_n and q -exponents for critical frequencies in the BM phase, while $\nu_m < \nu_a$ (spectrum 2).

| | ν_{m2} | ν_{a2} |
|---------|--|--|
| f_n | $\left(\frac{C_2 h_2}{C_{5/2} h_{5/2}}\right)^2$ | $\left(\frac{C_{(1-p)/2} h_{(1-p)/2}}{C_{5/2} h_{5/2}}\right)^{\frac{2}{4+p}}$ |
| q_ξ | -2 | $\frac{4-2p}{4+p}$ |
| q_e | 2 | $\frac{2(p-1)}{4+p}$ |
| q_B | $\frac{1}{2}$ | $\frac{p+2}{2(4+p)}$ |
| q_n | 0 | $\frac{8}{(4+p)(4-k)}$ |
| q_E | $\frac{1}{2}$ | $\frac{8+4p-kp-6k}{2(4+p)(4-k)}$ |
| q_t | $-\frac{3}{2}$ | $\frac{3kp-2k-12p-8}{2(4+p)(4-k)}$ |
| q_z | $\frac{1}{2}$ | $\frac{10k+4p-24-kp}{2(4+p)(4-k)}$ |

Table 11. f_n and q -exponents for critical frequencies in the ST phase, while $\nu_a < \nu_m$ (spectrum 1). The expressions contained in f_n need to be evaluated using the formulas applicable to the ST regime.

| | ν_{a1} | ν_{m1} |
|---------|--|---|
| f_n | $\left(\frac{C_{1/3} h_{1/3}}{C_2 h_2}\right)^{3/5}$ | $\left(\frac{C_{(1-p)/2} h_{(1-p)/2}}{C_{1/3} h_{1/3}}\right)^{\frac{6}{3p-1}}$ |
| q_ξ | $\frac{8}{5}$ | -2 |
| q_e | -1 | 2 |
| q_B | $\frac{1}{5}$ | $\frac{1}{2}$ |
| q_n | $\frac{5}{5-k}$ | $-\frac{5}{2(5-k)}$ |
| q_E | $-\frac{5+4k}{5(5-k)}$ | $\frac{10-k}{2(5-k)}$ |
| q_t | $\frac{30-16k}{5(5-k)}$ | $\frac{4k-15}{5-k}$ |
| q_z | $\frac{21k-55}{5(5-k)}$ | $\frac{10-3k}{5-k}$ |

Table 12. f_n and q -exponents for critical frequencies in the ST phase, while $\nu_m < \nu_a$ (spectrum 2).

| | ν_{m2} | ν_{a2} |
|---------|--|--|
| f_n | $\left(\frac{C_2 h_2}{C_{5/2} h_{5/2}}\right)^2$ | $\left(\frac{C_{(1-p)/2} h_{(1-p)/2}}{C_{5/2} h_{5/2}}\right)^{\frac{2}{4+p}}$ |
| q_ξ | -2 | $\frac{4-2p}{4+p}$ |
| q_e | 2 | $\frac{2(p-1)}{4+p}$ |
| q_B | $\frac{1}{2}$ | $\frac{p+2}{2(4+p)}$ |
| q_n | $-\frac{5}{2(5-k)}$ | $\frac{30-5p}{2(4+p)(5-k)}$ |
| q_E | $\frac{10-k}{2(5-k)}$ | $\frac{10p-kp-6k}{2(4+p)(5-k)}$ |
| q_t | $\frac{4k-15}{5-k}$ | $\frac{10-8k-15p+4kp}{(4+p)(5-k)}$ |
| q_z | $\frac{10-3k}{5-k}$ | $\frac{12k+10p-30-3kp}{(4+p)(5-k)}$ |

For clearer presentation we have labelled as ν_{a1} and ν_{m1} the critical frequencies ν_a and ν_m , respectively, when $\nu_a < \nu_m$ (i.e. when spectrum 1 applies), while they are labelled as ν_{a2} and ν_{m2} in the opposite case when spectrum 2 applies.

4.3 Evolution of critical parameters

A practical way of describing the temporal evolution of the parameters needed to construct a spectrum at any point is that of a smoothly broken power law. We can use equation (22), this time characterizing a temporal break in the following manner:

$$\Phi(t_{\text{obs}}) = A \left[\left(\frac{t_{\text{obs}}}{t_0}\right)^{-a_1 s_t} + \left(\frac{t_{\text{obs}}}{t_0}\right)^{-a_2 s_t} \right]^{-1/s_t}, \quad (27)$$

where (t_0, A) is the meeting point of the asymptotes and Φ is the value of any of the critical parameters. In this version of equation (22), a_1 and a_2 are the BM and ST slopes, respectively. We can rewrite the above equation in the following way:

$$\Phi(t_{\text{obs}}) = \left(\Phi_{\text{BM}}^{-s_t} + \Phi_{\text{ST}}^{-s_t} \right)^{-1/s_t}, \quad (28)$$

where both Φ_{BM} and Φ_{ST} have to be evaluated at t_{obs} .

In the previous sections we have established not only the scalings of the critical parameters we wish to follow, but also their actual values as a function of observer time in both extreme dynamical regimes. This allows us to insert them directly into equation (28), where the only unknown left is the sharpness s_t . As in the case of spectral breaks we have performed χ^2 -minimization fitting in logarithmic space and have arrived at a description of ‘ s_t ’ in terms of a polynomial of the following form:

$$s_t = s_0 + s_p p + s_{pp} p^2 + s_k k + s_{kk} k^2. \quad (29)$$

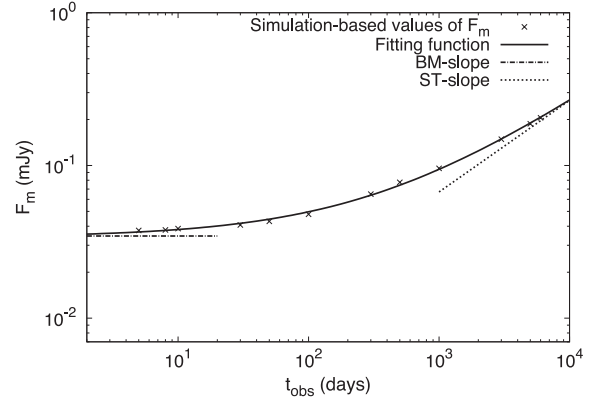
Results for the values of these s_t -factors are presented in Table 13.

An example fit of F_m is shown in Fig. 4. The behaviour of F_m displays clear deviations from the BM scalings already before 100 d observer time, for $E_{52} = 10^{52}$ erg, $n_0 = 1$ and $k = 0$. It settles to values sufficiently close (within 10 per cent) to the ST solution at around 5000 d. The *duration* of the transrelativistic regime is represented in s_t , for a given set of physical parameters. Table 13 demonstrates that the sharpness of every parameter is generally unique. Based on that we conclude that duration and features of the transrelativistic phase will be manifested differently across the spectrum.

Table 13. s_t -factors for the evolution of critical parameters. Numerically determined s_t -factors (see equation 29) describing the evolution of critical parameters (break frequencies and maximum flux) from the BM to the ST phase. Each column describes a specific parameter, the name of which is denoted on top.

| | F_m | ν_{a1} | ν_{a2}^a | ν_{m1} | ν_{m2} |
|----------|-------|------------|--------------|------------|------------|
| s_0 | -1.49 | -0.61 | 22.50 | -0.89 | 0.43 |
| s_p | 0.09 | 0 | -5.00 | 1.12 | 0 |
| s_{pp} | 0 | 0 | 0 | -0.21 | 0 |
| s_k | -0.76 | -0.12 | -2.00 | 0.14 | 0 |
| s_{kk} | 0.12 | -0.02 | 0 | 0 | 0 |

^aThe s -factors for ν_{a2} have not been determined by solving the system of equations resulting from measuring its value in different models but comprise a rather heuristic approach that minimizes the deviations from the numerically determined values.

**Figure 4.** A broken power-law fit to the evolution of F_m . Plotted are the BM and ST asymptotes. Simulation-based data have the following model parameters: $E_{52} = 1, n_0 = 1, p = 2.5, k = 0, \xi = 10^{-2}, \epsilon_e = 10^{-1}, \epsilon_B = 10^{-2}, d_{28} = 1, z = 0.56$.

4.4 Evolution of the sharpness of spectral breaks

Our findings so far enable us to determine the values of the critical frequencies and F_m at any given time for a burst of given physical properties. This allows for an accurate calculation of the flux at any given power-law segment of the spectrum. What is left to specify is the flux close to a spectral break for a general t_{obs} . To achieve that we need to provide a quantitative description for the evolution of the sharpness of spectral breaks from the BM to the ST phase.

As it turns out the sharpness of every spectral break follows a ‘characteristic path’ as it evolves from the relativistic values to the Newtonian ones. This path is qualitatively independent of the physical properties of the burst and is unique for every spectral break. In Fig. 5 we present these paths for all possible breaks. From the data gathered we have identified three time-scales that are represented in this figure: t_i, t_{NR} and t_f . In fact, we can simplify things further by setting $t_i = t_{\text{NR}}/100$ and $t_f = 10 t_{\text{NR}}$ which is generally valid up to a few per cent, regardless of the physical parameters of a burst.

Determination of t_{NR} carries (as in the case of fluxes and critical frequencies) an analytic and a numerical component. The analytic

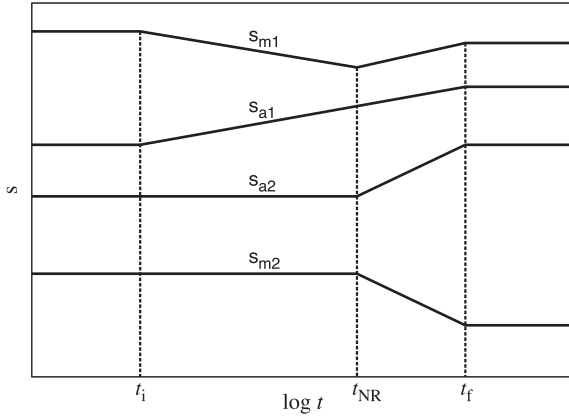


Figure 5. Evolution of sharpness for all possible spectral breaks. Before t_i and after t_f , s resumes its standard BM and ST values. The sharpness of the break around ν_{m1} shows the most complex pattern, by declining initially during the transrelativistic regime and then rising again to meet its ST asymptote. The value of s_{m1} at t_{NR} is ~ 0.18 smaller than the BM value.

part is motivated by considerations of the dynamics and is similar to other estimates of an observer time marking the transition to the Newtonian phase (Livio & Waxman 2000; Piran 2004). Specifically it is identified as the observer time at which the shock Lorentz factor drops to the value of 2, following the BM solution:

$$t_{NR} \sim \frac{8^{\frac{k-4}{3-k}}}{4-k} A_{NR}^{\frac{1}{3-k}} (1+z), \quad (30)$$

where $A_{NR} = \left[\left(\frac{17}{8\pi m_p} \right) c^{k-5} E_{52} n_0^{-1} \right]$.

Including the numerical calibration the expression for t_{NR} takes the form

$$t_{NR} = 10^{13.66} \frac{8^{\frac{k-4}{3-k}}}{4-k} A_{NR}^{\frac{1}{3-k}} (1+z) d. \quad (31)$$

Like all other time-scales describing a transition from BM to ST, t_{NR} scales as $(E_{52}/n_0)^{1/(3-k)} (1+z)$, as we expect from dimensional analysis (van Eerten & MacFadyen 2012). The same holds for t_0 appearing in equation (27) for all critical spectrum parameters. However, the actual value of t_0 for every parameter is influenced by the flux-calibrating polynomials C_{pol} (equation 19) and is therefore in general unique.

The equations, tables and plots of Sections 3 and 4 carry all the information necessary to construct a spectrum at any given time, based on given values for the relevant physical parameters that we have discussed in this work. In the following section we demonstrate how these results can be used to calculate the observed flux at any given frequency and time.

5 USING THE PRESCRIPTIONS

In this section we focus on the practical side of this work which is to construct spectra at any given observer time based on values for the physical parameters of a burst. These parameters we repeat here for clarity: E_{52} (isotropic blast-wave energy in units of 10^{52} erg), n_0 (number density at 10^{17} cm), p (index of the electron power-law distribution), k (index of the density distribution of the matter surrounding the burster), ξ (fraction of accelerated electrons), ϵ_e and ϵ_B (fractions of internal energy assigned to the relativistic electrons and magnetic field, respectively), ν_{obs} and t_{obs} (frequency and time of observation), and d_{28} and z (luminosity distance in units of 10^{28} cm and redshift).

The task of constructing a spectrum out of the presented formulas can be divided into four parts. The first is to obtain the values of the critical frequencies and the maximum flux at a given observer time. The next step is to determine the shape of the spectrum and its general characteristics, i.e. values of the flux away from the breaks, for each of the two possible spectra. The third step is to assign the appropriate sharpness parameters to all spectral breaks. The fourth and final step is to use equations (32) and (37) in order to calculate the observed flux at a given frequency.

Each of the two spectra is described by a single equation, at a given observer time. This equation should essentially represent a mathematical formulation of a double-broken power law. One of the ways to achieve that (Granot & Sari 2002) is to use a heuristic formula that combines equation (22) with a factor that assigns a second break at a different frequency. Then the whole spectrum can be described by the following expression:

$$F_\nu(\nu_{obs}) = A \left[\left(\frac{\nu_{obs}}{\nu_0} \right)^{-a_1 s} + \left(\frac{\nu_{obs}}{\nu_0} \right)^{-a_2 s} \right]^{-1/s} \times \left[1 + \left(\frac{\nu_{obs}}{\nu_1} \right)^{h(a_2-a_3)} \right]^{-1/h}. \quad (32)$$

The first two terms on the right-hand side of the above equation describe the first break as usual, while the third term describes the second break. We have introduced ν_1 , the frequency of the second break, a_3 , the slope of the third power-law segment, and h , the sharpness of the second break.

Equation (32) is exact only when the two breaks of the spectrum are sufficiently away from each other so that the power law connecting them is apparent, even for a small range of frequencies. When this is not the case, this equation provides an approximation to the real spectrum (Granot & Sari 2002).

In Fig. 6 we present a flowchart of the basic steps towards creating a spectrum of the emitted radiation at any given observer time. The details of each step can be found in the following subsections of the text.

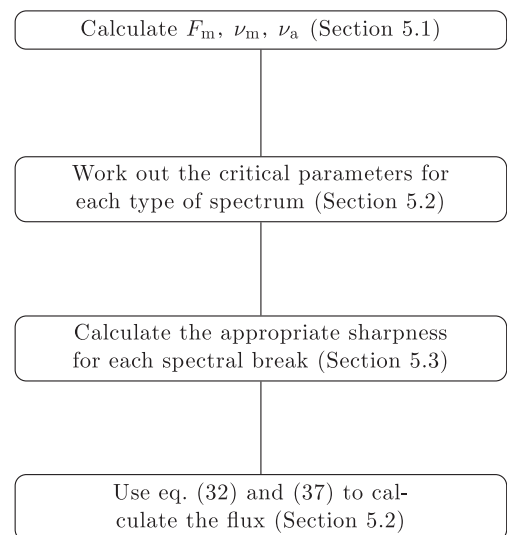


Figure 6. Flowchart showing the basic steps of the presented method. References are given to specific sections of the paper where the steps are described in more detail.

5.1 Values of F_m , ν_m and ν_a

In order to decide which of the two possible synchrotron spectra is valid (see Figs 1 and 2) one needs to calculate ν_{a1} , ν_{a2} , ν_{m1} and ν_{m2} . While all these frequencies can in principle be calculated independently, we opt for a different method. Requiring that the flux at both ends of the spectrum (in the power laws ν^2 and $\nu^{1-p/2}$) be the same regardless of the type of spectrum, one can show that only three of the four frequencies are independent. The relation between them is

$$\nu_{a2} = \nu_{a1}^{\frac{10}{3(4+p)}} \nu_{m1}^{\frac{3p-1}{3(4+p)}} \nu_{m2}^{\frac{1}{4+p}}. \quad (33)$$

We have expressed ν_{a2} in terms of the others because its transrelativistic profile is the one deviating more from the broken power-law approach. This way inconsistencies that may arise during a spectral transition, due to the overspecification of the evolution of the spectrum, are avoided and the fluxes in the leftmost and rightmost power laws are independent of the ordering of the critical frequencies.

Equation (28) should be used to calculate ν_{a1} , ν_{m1} and ν_{m2} for a given set of physical parameters and for the same observer time, before applying equation (33) to obtain ν_{a2} . $\Phi_{\text{BM}}(t_{\text{obs}})$ and $\Phi_{\text{ST}}(t_{\text{obs}})$ assume the corresponding forms of the critical frequencies, as those are expressed in equation (26) and Tables 9–12. The value of s_i is given by equation (29) and the relevant entries of Table 13.

Equation (28) should also be used to calculate F_m at the same observer time as the critical frequencies. The asymptotic expressions are presented in equation (24) and (25) and are to be evaluated using equation (19) and Table 8. Having found the values of all five critical parameters at the same observer time, we can now start constructing the spectrum.

5.2 Shape and flux normalization of the spectrum

In the case of spectrum 1 the characteristic synchrotron frequency ν_{m1} lies on the optically thin part of the spectrum. Consequently, its value is affected by radiation from the whole blast wave. In the case of spectrum 2 self-absorption allows only for the front to contribute to the flux close to ν_{m2} . In practice the values of ν_{m1} and ν_{m2} are always close to each other (within the same order of magnitude). Therefore, we conclude that the location of ν_m on the spectrum is mostly determined by the conditions at the front and is only slightly affected by what the optical depth of the blast wave is at that frequency.

On the other hand, values of ν_{a1} and ν_{a2} can differ substantially with respect to each other. However, in most cases they will both be either smaller or bigger than ν_{m1} and ν_{m2} . We will be referring to these cases as definite ordering, whereas all other cases will be referred to as indefinite ordering. When $\nu_{a1}, \nu_{a2} < \nu_{m1}, \nu_{m2}$ the spectrum will have the form of Fig. 1 (spectrum 1), while if $\nu_{m1}, \nu_{m2} < \nu_{a1}, \nu_{a2}$ the spectrum will have the form of Fig. 2 (spectrum 2). In the case of indefinite ordering, the actual positions of the two critical frequencies on the spectrum are very close to each other signalling a spectral transition, typically from spectrum 1 to spectrum 2. In terms of observer time, the time-span of this transition is relatively small. Let t_{tr} be the observer time when indefinite ordering sets in. The duration of this transition (time-span of indefinite ordering) is typically a fraction of t_{tr} . During that time the choice of critical frequencies affects the flux across the spectrum by factors of the order of unity.

In practice, it is preferable to always take the values suggested by both spectra into account, through a consistent weighing method. This way glitches that may appear in the produced light curves

when switching from one spectrum to another are avoided. Instead, the light curves' behaviour smoothly progresses from the early-time spectrum 1 configuration to the late-time spectrum 2. The weight of each spectrum is represented by a power-law dependence in time that contains a characteristic time-scale t_{flip} related to the observer time at which the spectrum is transitioning from spectrum 1 to spectrum 2. This characteristic time-scale can be estimated numerically by solving equation (27) for both t_{T1} (the time at which $\nu_{m1} = \nu_{a1}$) and t_{T2} (the time at which $\nu_{m2} = \nu_{a2}$), and defining

$$t_{\text{flip}} = f_{\text{flip}} \times \max(t_{\text{T1}}, t_{\text{T2}}). \quad (34)$$

We have found that the value of f_{flip} that results in smaller deviations across the parameter space of $[p, k]$ is 1.6.

The weights of spectra 1 and 2 can be written as

$$W_1 = \frac{(t_{\text{obs}}/t_{\text{flip}})^{-1}}{(t_{\text{obs}}/t_{\text{flip}})^{-1} + (t_{\text{obs}}/t_{\text{flip}})}, \quad (35)$$

$$W_2 = \frac{(t_{\text{obs}}/t_{\text{flip}})}{(t_{\text{obs}}/t_{\text{flip}})^{-1} + (t_{\text{obs}}/t_{\text{flip}})}. \quad (36)$$

The flux at a given frequency will then be

$$\log F = W_1 \times \log F_1 + W_2 \times \log F_2, \quad (37)$$

where F_1 and F_2 are the fluxes calculated at that frequency through spectra 1 and 2 (see Sections 5.2.1 and 5.2.2), respectively.

5.2.1 Spectrum 1: $\nu_a < \nu_m$

This is the asymptotic case where both ν_{a1} and ν_{a2} are smaller than ν_{m1} and ν_{m2} . Consequently the positions of the critical frequencies are given by $\nu_a = \nu_{a1}$ and $\nu_m = \nu_{m1}$. The parameters of equation (32) get the following values:

- (i) $\nu_0 = \nu_{a1}$
- (ii) $\nu_1 = \nu_{m1}$
- (iii) $A = F_m(\nu_0/\nu_1)^{1/3}$
- (iv) $a_1 = 2$
- (v) $a_2 = 1/3$
- (vi) $a_3 = (1 - p)/2$

5.2.2 Spectrum 2: $\nu_m < \nu_a$

For spectrum 2 in the asymptotic limit both ν_{a1} and ν_{a2} are bigger than ν_{m1} and ν_{m2} . Thus, the positions of the critical frequencies are given by $\nu_m = \nu_{m2}$ and $\nu_a = \nu_{a2}$. However, in spectrum 2 the flux at ν_m is not F_m ; that would be the case if it were not for absorption. We can use this fact to first calculate the flux at ν_a . Although in the present spectrum configuration the actual position of ν_m is given by ν_{m2} , it is ν_{m1} that we should use for obtaining the flux at ν_a . The variables become:

- (i) $\nu_0 = \nu_{m2}$
- (ii) $\nu_1 = \nu_{a2}$
- (iii) $A = F_m \left(\frac{\nu_{a2}}{\nu_{m1}} \right)^{(1-p)/2} \left(\frac{\nu_{m2}}{\nu_{a2}} \right)^{2.5}$
- (iv) $a_1 = 2$
- (v) $a_2 = 2.5$
- (vi) $a_3 = (1 - p)/2$

5.3 Sharpness parameters of spectral breaks

The only two parameters left to specify in equation (32) are s and h , the sharpness of the first and the second break in the spectrum, respectively. In order to assign the proper sharpness to each break we first have to compare t_{obs} to t_{NR} (see equation 31). There are four distinct cases, as illustrated in Fig. 5.

5.3.1 $t_{\text{obs}} < t_i$

In this case all sharpness parameters attain their BM values as these are given in Table 6.

5.3.2 $t_{\text{obs}} > t_f$

In this case all sharpness parameters attain their ST values as these are given in Table 7.

5.3.3 $t_i < t_{\text{obs}} < t_{\text{NR}}$

In this case breaks ν_{m2} and ν_{a2} retain their BM sharpness. The other two exhibit some evolution towards the corresponding ST values. The sharpness around ν_{m1} will be

$$s_{m1} = 0.09 \log \left(\frac{t_i}{t_{\text{obs}}} \right) + s_i, \quad (38)$$

where s_i is the sharpness of the particular break in the BM regime.

The sharpness around ν_{a1} will be

$$s_{a1} = \frac{(s_f - s_i)}{3} \log \left(\frac{t_{\text{obs}}}{t_i} \right) + s_i, \quad (39)$$

where s_i and s_f are the sharpness parameters at the BM and ST phases, respectively.

5.3.4 $t_{\text{NR}} < t_{\text{obs}} < t_f$

In this final case all breaks exhibit a sharpness evolving towards its ST value. For ν_{m1} the sharpness will be given by

$$s_{m1} = (s_f - s_i + 0.18) \log \left(\frac{t_{\text{obs}}}{t_f} \right) + s_f, \quad (40)$$

while for ν_{a1} the value of the sharpness is still given by equation (39).

The sharpness around ν_{a2} will be given by

$$s_{a2} = (s_f - s_i) \log \left(\frac{t_{\text{obs}}}{t_{\text{NR}}} \right) + s_i, \quad (41)$$

while for ν_{m2} we find a similar result:

$$s_{m2} = (s_f - s_i) \log \left(\frac{t_{\text{obs}}}{t_{\text{NR}}} \right) + s_i. \quad (42)$$

5.4 Examples of results

We have described a practical implementation of our results to construct spectra at any given time, based on values for the physical quantities characterizing the burst. We now show comparisons between simulation-generated spectra and spectra that have been constructed using the provided flux prescriptions.

In Fig. 7 a comparison between a simulation-based spectrum and an analytic one is shown. In all power-law segments and the linking breaks, the flux prediction is never more than 10 per cent off

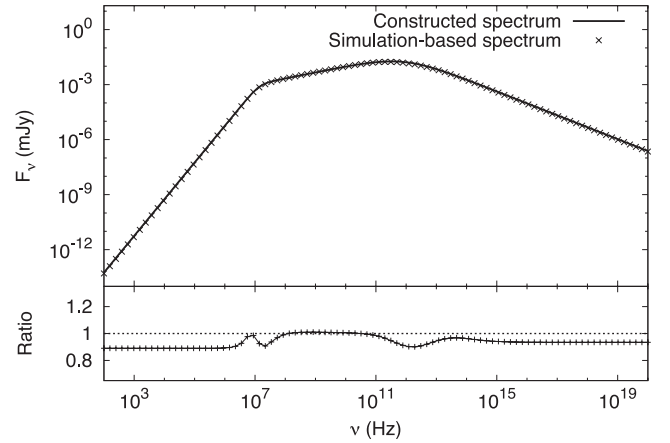


Figure 7. A typically good match between an analytically constructed spectrum and one based on a simulation. Both are taken at 100 d. ν_a lies at $\sim 10^7$ Hz and ν_m at $\sim 10^{12}$ Hz. Model parameters for both spectra are as follows: $E_{52} = 1$, $n_0 = 1$, $p = 2.3$, $k = 0$, $\xi = 10^{-2}$, $\epsilon_e = 10^{-1}$, $\epsilon_B = 10^{-2}$, $d_{28} = 1$, $z = 0.56$.

compared to the simulation-based data. We can translate these deviations into relative errors for the values of the physical parameters. This we do by adjusting their values so that those deviations vanish in particular regimes of the spectrum. For the blast-wave energy (E_{52}) the error ranges from 3 to 15 per cent depending on which power-law segment (or spectral break) one uses for the comparison. In the case of n_0 the maximum error is 15 per cent. For p the difference is of the order of 0.05, while for k it is of the order of 0.08. For ϵ_e and ϵ_B the error is of the order of 10 per cent while for ξ it reaches up to 30 per cent.

In Fig. 8 we present another comparison between a simulation-based spectrum and a constructed one. This one was chosen for exhibiting one of the largest deviations we have encountered. While the self-absorbed part of the spectrum is matched well by the constructed spectrum, flux in the $\nu^{(1-p)/2}$ segment differs by ~ 25 per cent. The corresponding errors in the derivation of values for physical quantities are the following: up to 16 per cent for E_{52} , up to 10–90 per cent for n_0 (flux in the $\nu^{(1-p)/2}$ segment depends very weakly on n_0 for these model parameters), up to 35 per cent for ξ ,

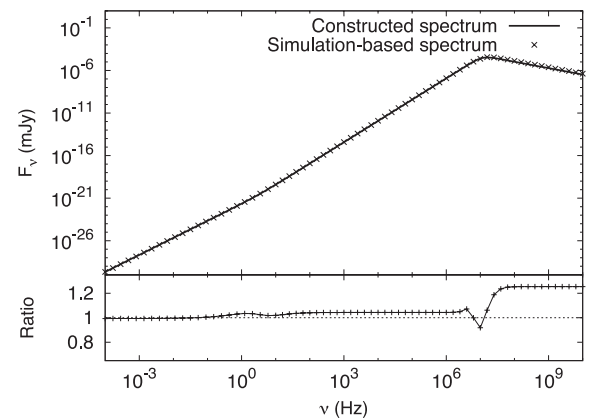


Figure 8. An example of a constructed spectrum that shows relatively large deviations from the numerical result in the optically thin part of the spectrum. Both spectra are taken at 500 d. ν_m lies at ~ 1 Hz and ν_a at $\sim 10^7$ Hz. Model parameters are as follows: $E_{52} = 1$, $n_0 = 1$, $p = 2.5$, $k = 0.5$, $\xi = 1$, $\epsilon_e = 10^{-4}$, $\epsilon_B = 10^{-2}$, $d_{28} = 1$, $z = 0.56$.

15 per cent for ϵ_e and 30 per cent for ϵ_B , while for p and k we find differences up to 0.1 and 0.2, respectively.

We stress that these deviations are not with respect to a best-fitting value but are indicative of how much every parameter should be tweaked to match fluxes in individual power-law segments of the spectrum. More often than not such a tweak would actually produce a rather bad fit overall. Thus the deviations we have listed may be viewed as an upper limit to what a broad-band fit would produce.

5.5 Application to mildly relativistic outflows

Recently Nakar & Piran (2011) have discussed the radio signal following the ejection of spherical, Newtonian or mildly relativistic outflows expected from binary NS mergers. They estimate that due to the low initial Lorentz factors of these outflows, their deceleration (and entry to the ST phase) will be manifested at $t_{\text{dec}} \sim 60$ d observer time, for $E_{52} = 0.01$, $n_0 = 1$, $k = 0$, $\beta_i \sim 1$ (initial velocity). This is also the time at which optically thin emission at $\nu_{\text{obs}} = 5$ GHz will peak in the range 0.01–0.1 mJy, for a distance of the source in the range 1–3 Gpc. Here, we test these estimates using the prescriptions presented in this paper.

The model we have developed in this study is based on (and therefore, applicable to) outflows that are initially ultrarelativistic. Thus, it is not obvious that it can be used to model non-relativistic outflows. Order-of-magnitude calculations in the lab frame can illustrate the limitations. A relativistic outflow of coasting Lorentz factor Γ_i will slow down after sweeping mass Γ_i times smaller than the mass of the ejecta (Rees & Mészáros 1992). This will happen at a time

$$t_{\text{BM}} = \left(\frac{3E}{4\pi\rho_1 c^5} \right)^{1/3} \Gamma_i^{-2/3}. \quad (43)$$

From that point onwards the outflow will decelerate according to the BM solution ($\Gamma \propto t^{-3/2}$) becoming Newtonian ($\Gamma \sim 1$) at

$$t_{\text{N}} = \left(\frac{3E}{4\pi\rho_1 c^5} \right)^{1/3}. \quad (44)$$

The corresponding radius is

$$r_{\text{N}} = t_{\text{N}} c. \quad (45)$$

Equations (44) and (45) effectively mark the onset of the ST phase.

In the case of subrelativistic and mildly relativistic outflows the deceleration time (also marking the transition to the ST phase) occurs when the swept mass is comparable to the rest mass of the ejecta:

$$t_{\text{dec}} = \left(\frac{3E}{2\pi\rho_1 c^5} \right)^{1/3} \beta_i^{-5/3}. \quad (46)$$

At t_{dec} the shock is at a radius

$$r_{\text{dec}} = \beta_i t_{\text{dec}} c. \quad (47)$$

From equations (44)–(47) it is clear that as $\beta_i \rightarrow 1$ the onset of the ST phase for Newtonian outflows approaches that of the relativistic analogue with the same energy. This implies that fast ($v \sim c$) outflows (regardless of the Lorentz factor) have no *memory* of their history from t_{dec} onwards. Therefore we can apply the ST scalings of the flux prescriptions to a mildly relativistic outflow (as the one considered by Nakar & Piran 2011) at observer times $t_{\text{obs}} \geq t_{\text{dec}}$. In the subrelativistic case ($\beta_i \ll 1$) equations (46) and (47) imply that the outflow will decelerate later and at a greater radius. Nevertheless, the ST scalings of the flux prescriptions apply at

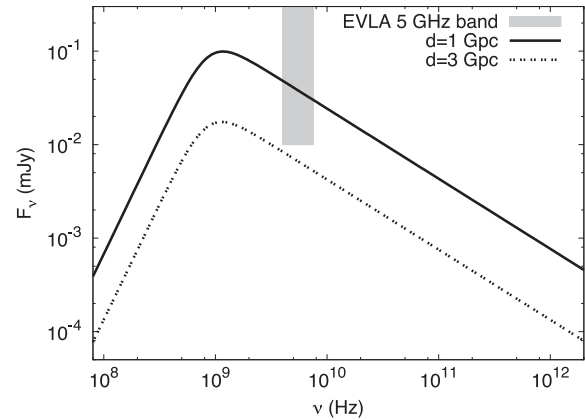


Figure 9. Synchrotron spectra of a mildly relativistic outflow at distances of 1 and 3 Gpc, taken at 60 d observer time. The grey shaded area represents the 5 GHz band of the EVLA with a bandwidth of 3.5 GHz and a 4σ detection threshold of ~ 10 μ Jy for 1-h integration (Perley et al. 2011). The value of p for both spectra is 2.5. The other physical parameters have the following values: $E_{52} = 0.01$, $n_0 = 1$, $k = 0$, $\xi = 1$, $\epsilon_e = \epsilon_B = 0.1$.

observer times $t_{\text{obs}} \gg t_{\text{dec}}$, i.e. sufficiently later than the deceleration time.

For the application to mildly relativistic outflows we have set $E_{52} = 0.01$, $n_0 = 1$, $k = 0$ for the macroscopic parameters of the blast wave and its environment and $\xi = 1$, $\epsilon_e = \epsilon_B = 0.1$, for the microphysics, while $\nu_{\text{obs}} = 5$ GHz and $t_{\text{obs}} = 60$ d. The electron spectral index p is varied within the range 2.1–3.0, while for the distance we have taken the two extreme values of 1 and 3 Gpc.

In accordance with Nakar & Piran (2011) we find that ν_{obs} is in the optically thin part of the spectrum for all cases. In this regime the flux increases monotonically for an increasing p and for $p = 3.0$ it is about four times higher than the $p = 2.1$ case. For $d_{28} = 0.31$ (~ 1 Gpc) the flux at 5 GHz lies in the range 0.015–0.06 mJy, depending on the value of p . At $d_{28} = 0.93$ (~ 3 Gpc) we find the flux to be always below 0.01 mJy, albeit marginally for relatively high values of p . This is illustrated in Fig. 9 where two spectra are shown corresponding to distances of 1 and 3 Gpc. They are both taken at $t_{\text{obs}} = 60$ d, for a characteristic value of $p = 2.5$.

Binary NS mergers are believed to be the progenitors of short GRBs (see Nakar 2007 and references therein) and are observed in a variety of environments, such as elliptical, spiral and irregular galaxies (Berger 2009). A considerable fraction of them, however, appear to be hostless, occurring in the intergalactic medium and thus surrounded by a much more tenuous gas than that commonly found inside galaxies (Berger 2010). We have repeated the calculation of the spectrum from a spherical outflow resulting from a NS–NS merger for a surrounding medium of density $n_0 = 10^{-3} \text{ cm}^{-3}$, where the lower density results in a later onset of the ST phase at ~ 400 d. Keeping all other parameters constant we find that the radio signal at 5 GHz will be detectable by the EVLA up to a distance of ~ 100 Mpc.

The implication of these results is that moderately energetic outflows ($E = 10^{50}$ erg) expected to accompany NS–NS mergers (Rezzolla et al. 2011) can produce synchrotron radiation detectable by the EVLA from distances up to ~ 1 Gpc, larger than the detection horizon of the upcoming versions of gravitational-wave detectors (Nakar & Piran 2011). This assumes that the density of the matter surrounding the merger is of the order of 1 cm^{-3} . These radio signals will peak at time-scales of the order of a few months, if the corresponding outflows have initial velocities close to the speed of light.

In the case of more tenuous circumburst media the ST time-scale grows and the detection horizon of the EM signal drops accordingly. The presented flux prescriptions are applicable throughout the ST phase of these outflows.

6 DISCUSSION

We present analytic flux prescriptions for broad-band synchrotron spectra originating from GRB outflows, suitable for fast and detailed modelling of the afterglow phase. They are applicable throughout the evolution of observed afterglows, during which external shocks are the dominant source of particle acceleration, and account for the exact shape of the synchrotron spectrum, including self-absorption, but ignoring cooling. These prescriptions are based on high-resolution, 1D hydrodynamic simulations performed using the adaptive-mesh-refinement code *AMRVAC*. To obtain spectra we have employed a radiation code that solves the equation of radiative transfer through the evolving blast wave as this is determined by the simulations. The presented formulas carry two components. The first is derived analytically and expresses the dependence of the flux on relevant physical parameters (E_{52} , n_0 , p , k , ξ , ϵ_e , ϵ_B , v_{obs} , t_{obs} , d_{28} , z), while the second component reflects the calibration that the results of simulations have introduced to the flux levels.

For each asymptotic dynamical regime (BM and ST) we provide prescriptions for the flux at every power-law segment but also at frequencies close to spectral breaks. These are modelled as smoothly broken power laws with the sharpness of the break given in terms of the structure of the surrounding medium (k) and the electron distribution (p). During the transrelativistic regime we find that the values of critical frequencies (ν_m , ν_a) and peak flux (F_m) of the synchrotron spectrum show a gradual transition from the asymptotic power-law behaviour in the BM phase to the corresponding one in the ST phase. This fact has allowed us to model their temporal profiles as smoothly broken power laws. For every parameter (F_m , ν_m and ν_a) we provide formulas describing the sharpness of these breaks in terms of p and k . In order to model the evolution of a spectral break's sharpness, we have recognized the unique pattern that each break exhibits. We have introduced t_{NR} whose derivation is based on considerations of the outflow dynamics. The result is a set of analytic expressions that extend the applicability of the flux prescriptions to any given observer time.

An element of this study worth emphasizing is the inclusion of k (representing the structure of the circumburst medium) as a fitting parameter. This is motivated by the fact that environments of stars with variable mass-loss rates (such as massive stars, prime candidates for long GRB progenitors) can have structures more complex than the usually assumed $k = 0$ or 2 (Ramirez-Ruiz et al. 2005) and fits using k as a free parameter do not exclude such a possibility (Yost et al. 2003; Curran et al. 2009). As can be seen in Tables 3 and 5 the impact of k on flux values is modest and varies smoothly across a plausible range of k -values $[0, 2]$. Nevertheless, its effect is measurable in light of the provided formulas, contributing an extra tool to afterglow fitting and addressing the nature of GRB progenitors.

Beyond the context of GRBs, the provided prescriptions are useful for modelling synchrotron emission from spherical adiabatic blast waves of arbitrary velocity (with the limitations analysed in Section 5.5) as long as they have swept up enough mass to be decelerating. Obvious applications include Type Ibc supernovae (Soderberg et al. 2010), often associated with GRBs (Woosley & Bloom 2006) and mildly relativistic or subrelativistic spherical outflows from binary NS mergers. The latter are candidates for provid-

ing the EM counterpart (peaking at radio frequencies) to a possible signal of gravitational waves (Metzger & Berger 2012). By applying the ST scalings of the presented flux prescriptions on mildly relativistic outflows we show that prospects of detecting such radio signals from within the horizon of gravitational-wave detectors, LIGO (Abbott et al. 2009) and Virgo (Acernese et al. 2008), are realistic (Nakar & Piran 2011).

It is interesting to note that apart from the dependence on p and k , we have also found that the sharpness of a spectral break can be influenced to some extent by the microphysical parameters ϵ_e , ϵ_B and ξ . This has been particularly seen in spectral breaks that involve absorption. The reason for this is the dependence of the absorption coefficient on the chosen microphysics through equation (15). The microphysical parameters in effect regulate the physical depth of the blast wave corresponding to a given value of the optical depth. Therefore an increase/decrease of α'_v results in a less/more diverse sample of local electron distributions contributing to the flux across a spectral break and thus a sharper/smoother transition. We have chosen not to include the effect of the microphysics on the sharpness formulas, as it typically influences s by no more than 10–15 per cent (the flux to a lesser extent) and it would greatly complicate the heuristic equations we present.

Contrary to the approach on the evolution of a spectral break's sharpness, where the introduction of t_{NR} is useful, when describing the temporal evolution of the spectrum's critical parameters we deliberately choose not to use such a time-scale. The reason is that, as it turns out, there is no such thing as a single global time-scale applicable to the behaviour of all observable quantities. Instead, every critical parameter of the spectrum is characterized by its own break time, the meeting point of the BM and ST asymptotes. One can verify that by computing t_0 of equation (27) for a few critical parameters of the same model, by equating the asymptotic expressions. They will be found to differ by factors up to a few. This happens because at any given observer time all these parameters are affected by contributions of radiation from various parts of the outflow, emitted within a range of lab-frame times. For each parameter the weight of these contributions will differ, leading to the inference of contrasting time-scales by an observer. This stresses the need for models that can naturally account for this kind of features, by implementing accurate calculations of the blast-wave dynamics and the shape of the spectrum.

By inspection of Fig. 4 one can realize that the broken power-law approach is an approximation to the actual behaviour of any critical spectrum parameter during the transrelativistic phase. The parameter that exhibits the strongest deviation from this description is ν_{a2} . The reason for this can be traced to the behaviour of the flux in the optically thin part of the spectrum. An example of this behaviour is shown in Fig. 10, where a feature readily apparent is a smooth bump centred at ~ 500 d (this can also be seen in fig. 10 of van Eerten et al. 2010a). This introduces a similar feature in the temporal profile of ν_{a2} . As a result, the actual values of that frequency can deviate as much as ~ 15 per cent from the fitting function (smooth power-law break) at observer times relatively close to t_{NR} . This can have an effect on constructed light curves if the self-absorbed part of spectrum 2 is used and only during the transrelativistic phase. The impact on flux levels is stronger than the deviations shown in Fig. 10 because the flux at the ν^2 and $\nu^{5/2}$ segments of spectrum 2 scales as $\nu_{a2}^{-(p+4)/2}$. We therefore recommend using equation (33) in all cases as this method provides a more accurate and consistent way of constructing spectra and light curves.

By now there are a number of studies in the literature that present formulas calculating spectra from GRB afterglows. The importance

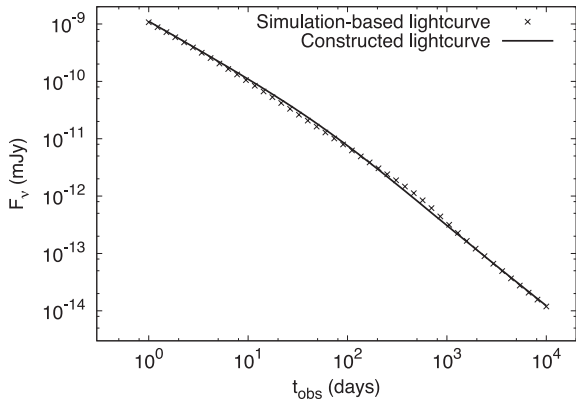


Figure 10. Simulation-based light curve taken at 10^{20} Hz (no cooling taken into account). A bump at ~ 500 d is apparent. For comparison we have plotted the constructed light curve based on the presented flux prescriptions. Model parameters are as follows: $E_{52} = 1$, $n_0 = 1$, $p = 2.3$, $k = 0$, $\xi = 1$, $\epsilon_e = 10^{-4}$, $\epsilon_B = 10^{-2}$, $d_{28} = 1$, $z = 0.56$.

of taking into account the blast-wave structure and the exact shape of the spectrum has been stressed by discrepancies in the derived values of physical parameters between simple (Wijers & Galama 1999) and more elaborate (Granot & Sari 2002; van Eerten & Wijers 2009) models. Inclusion of details regarding the shock structure can be done either analytically (in either of the two asymptotic regimes of the dynamics) or through the performance of simulations, as is done in the present work. The advantage of numerical simulations is that they cover the transrelativistic phase of the outflow and the level of detail they provide in all cases. The disadvantage is the price they come at, both in terms of time and resources.

In this paper we provide an efficient way of utilizing the benefits of simulations, as those are reflected on the presented analytic prescriptions. A similar approach has been taken by van Eerten & MacFadyen (2012), whose fitting method is based on the scale invariance of light curves. This method naturally accounts for features like sideways spreading of the jet and off-axis observation angles, features that only arise in simulations of at least two dimensions and cannot be captured in the context of this research. However, it requires the use of a large data base of light curves which does not yet exist. So far no study of the afterglow radiation using 2D hydrodynamic simulations (Zhang & MacFadyen 2009; Wygoda et al. 2011; De Colle et al. 2012) has resulted in the derivation of flux prescriptions. In fact this is the first time, even for the simple spherical case, that simulation-based flux prescriptions beyond the BM phase are presented. The box-fit method of van Eerten et al. (2012) does provide a fitting code but requires the use of a parallel computer network in order to fit data by iterating through a ‘box’ of simulations. Therefore, analytic flux prescriptions based on 1D simulations, as the ones presented here, can be the base for comparisons with future work in that direction based on 2D simulations. Moreover, 1D models are always relevant both at observer times before the jet-break (when most parts of the outflow are causally disconnected) and at late times when the outflow is roughly spherical and allow for accurate calorimetry of jetted outflows after the jet-break but well before spherical symmetry has been reached, as long as the observer is not far off-axis (Wygoda et al. 2011).

In all the simulations that we have performed to arrive at the presented flux prescriptions, the microphysical parameters have been kept constant throughout the run and at every part of the outflow. This is by no means guaranteed and therefore introduces an uncertainty in our results. An interesting topic for further study is

the implementation of evolving microphysical parameters and their effect on the flux prescriptions. Such an evolution is expected on theoretical grounds for some of those parameters (Granot, Königl & Piran 2006). A qualitative study of the evolution of ξ at the shock front and the evolution of ϵ_B downstream has already been presented in van Eerten et al. (2010a). Meanwhile, there is also growing amount of observational evidence for this process taking place in GRB afterglows (Panaitescu et al. 2006; Kong et al. 2010; Filgas et al. 2011). Incorporating effects like time dependence of the microphysics into flux prescriptions can extend the predictions of the standard fireball model and thus broaden the theoretical framework within which observations are currently being interpreted.

7 CONCLUSIONS

We have used high-resolution 1D hydrodynamic simulations to calibrate flux scalings of synchrotron, self-absorbed radiation for GRB afterglows in the relativistic and Newtonian dynamical phases (BM and ST, respectively). The transition from the former to the latter is well described by approximating the evolution of spectral parameters (maximum flux and positions of critical frequencies) by power-law breaks connecting the two asymptotic behaviours. The properties of these breaks have been modelled in terms of the values of the physical parameters describing the blast wave. This way we have managed to encapsulate the precision of the performed simulations into a set of analytic formulas that trace the full evolution of GRB afterglows, from the ultrarelativistic to the Newtonian phase. Due to the general nature of the prescriptions, they are applicable to any source characterized by emission of synchrotron radiation from an adiabatic blast wave.

A numerical code containing a practical implementation of the results presented in this paper combined with a fitting code is freely available on request and online at <http://www.astro.uva.nl/research/cosmics/gamma-ray-bursts/software/>.

ACKNOWLEDGMENTS

This research was supported by NOVA and in part by NASA through grant NNX10AF62G issued through the Astrophysics Theory Program and by the NSF through grant AST-1009863. RAMJW acknowledges support from the ERC via Advanced Investigator Grant No. 247295. We thank SARA Computing and Networking Services (www.sara.nl) for their support in using the Lisa Compute Cluster. We thank Evert Rol and Alexander van der Horst for useful discussions.

REFERENCES

- Abbott B. P. et al., 2009, *Rep. Prog. Phys.*, 72, 076901
- Acerese F. et al., 2008, *Class. Quantum Grav.*, 25, 184001
- Berger E., 2009, *ApJ*, 690, 231
- Berger E., 2010, *ApJ*, 722, 1946
- Beuermann K. et al., 1999, *A&A*, 352, L26
- Blandford R. D., McKee C. F., 1976, *Phys. Fluids*, 19, 1130
- Bloom J. S. et al., 2011, *Sci*, 333, 203
- Booth R. S., de Blok W. J. G., Jonas J. L., Fanaroff B., 2009, preprint (arXiv:0910.2935)
- Carilli C., Rawlings S., 2004, *New Astron. Rev.*, 48, 979
- Chevalier R. A., 1977, *ARA&A*, 15, 175
- Chevalier R. A., 1982, *ApJ*, 258, 790
- Costa E., Frontera F., Heise J. et al., 1997, *Nat*, 387, 783
- Curran P. A., Starling R. L. C., van der Horst A. J., Wijers R. A. M. J., 2009, *MNRAS*, 395, 580

- De Colle F., Granot J., López-Cámara D., Ramirez-Ruiz E., 2012, *ApJ*, 746, 122
- De Colle F., Ramirez-Ruiz E., Granot J., Lopez-Camara D., 2012, *ApJ*, 751, 57
- Draine B. T., McKee C. F., 1993, *ARA&A*, 31, 373
- Eichler D., Waxman E., 2005, *ApJ*, 627, 861
- Eichler D., Livio M., Piran T., Schramm D. N., 1989, *Nat*, 340, 126
- Filgas R. et al., 2011, *A&A*, 535, A57
- Frail D. A., Waxman E., Kulkarni S. R., 2000, *ApJ*, 537, 191
- Granot J., Sari R., 2002, *ApJ*, 568, 820
- Granot J., Piran T., Sari R., 1999, *ApJ*, 527, 236
- Granot J., Königl A., Piran T., 2006, *MNRAS*, 370, 1946
- Groot P. J. et al., 1997, *IAU Circ.*, 6584, 1
- Huang Y. F., Dai Z. G., Lu T., 1999, *MNRAS*, 309, 513
- Keppens R., Meliani Z., van Marle A., Delmont P., Vlasis A., van der Holst B., 2012, *J. Comput. Phys.*, 231, 718
- Kobayashi S., Piran T., Sari R., 1999, *ApJ*, 513, 669
- Kong S. W., Wong A. Y. L., Huang Y. F., Cheng K. S., 2010, *MNRAS*, 402, 409
- Livio M., Waxman E., 2000, *ApJ*, 538, 187
- Meliani Z., Sauty C., Tsinganos K., Vlahakis N., 2004, *A&A*, 425, 773
- Meliani Z., Keppens R., Casse F., Giannios D., 2007, *MNRAS*, 376, 1189
- Mészáros P., 2006, *Rep. Prog. Phys.*, 69, 2259
- Mészáros P., Rees M. J., 1993, *ApJ*, 405, 278
- Metzger B. D., Berger E., 2012, *ApJ*, 746, 48
- Metzger B. D., Giannios D., Mimica P., 2012, *MNRAS*, 420, 3528
- Morganti R. et al., 2011, preprint (arXiv:1112.5094)
- Nakar E., 2007, *Phys. Rep.*, 442, 166
- Nakar E., Piran T., 2011, *Nat*, 478, 82
- Paczyński B., Rhoads J. E., 1993, *ApJ*, 418, L5
- Panaitescu A., Kumar P., 2000, *ApJ*, 543, 66
- Panaitescu A., Mészáros P., Burrows D., Nousek J., Gehrels N., O'Brien P., Willingale R., 2006, *MNRAS*, 369, 2059
- Perley R. A., Chandler C. J., Butler B. J., Wrobel J. M., 2011, *ApJ*, 739, L1
- Piran T., 2004, *Rev. Mod. Phys.*, 76, 1143
- Ramirez-Ruiz E., García-Segura G., Salmonson J. D., Pérez-Rendón B., 2005, *ApJ*, 631, 435
- Rees M. J., Mészáros P., 1992, *MNRAS*, 258, 41P
- Rees M. J., Mészáros P., 1994, *ApJ*, 430, L93
- Rezzolla L., Giacomazzo B., Baiotti L., Granot J., Kouveliotou C., Aloy M. A., 2011, *ApJ*, 732, L6
- Rybicki G. B., Lightman A. P., 1986, *Radiative Processes in Astrophysics*. Wiley, New York, NY
- Sari R., Piran T., 1997, *ApJ*, 485, 270
- Sari R., Piran T., Narayan R., 1998, *ApJ*, 497, L17
- Sedov L. I., 1959, *Similarity and Dimensional Methods in Mechanics*. Academic Press, New York, NY
- Sironi L., Spitkovsky A., 2009, *ApJ*, 707, L92
- Soderberg A. M. et al., 2010, *Nat*, 463, 513
- Spitkovsky A., 2008, *ApJ*, 682, L5
- Syngé J. L., 1957, *The Relativistic Gas*. North-Holland Publishing Company, Amsterdam
- van Eerten H. J., MacFadyen A. I., 2012, *ApJ*, 747, L30
- van Eerten H. J., Wijers R. A. M. J., 2009, *MNRAS*, 394, 2164
- van Eerten H. J., Leventis K., Meliani Z., Wijers R. A. M. J., Keppens R., 2010a, *MNRAS*, 403, 300
- van Eerten H., Zhang W., MacFadyen A., 2010b, *ApJ*, 722, 235
- van Eerten H. J., Meliani Z., Wijers R. A. M. J., Keppens R., 2011, *MNRAS*, 410, 2016
- van Eerten H., van der Horst A., MacFadyen A., 2012, *ApJ*, 749, 44
- van Paradijs J., Kouveliotou C., Wijers R. A. M. J., 2000, *ARA&A*, 38, 379
- Wijers R. A. M. J., Galama T. J., 1999, *ApJ*, 523, 177
- Wijers R. A. M. J., Rees M. J., Mészáros P., 1997, *MNRAS*, 288, L51
- Woosley S. E., 1993, *ApJ*, 405, 273
- Woosley S. E., Bloom J. S., 2006, *ARA&A*, 44, 507
- Wygoda N., Waxman E., Frail D. A., 2011, *ApJ*, 738, L23
- Yost S. A., Harrison F. A., Sari R., Frail D. A., 2003, *ApJ*, 597, 459
- Zhang W., MacFadyen A., 2009, *ApJ*, 698, 1261

This paper has been typeset from a $\text{\TeX}/\text{\LaTeX}$ file prepared by the author.